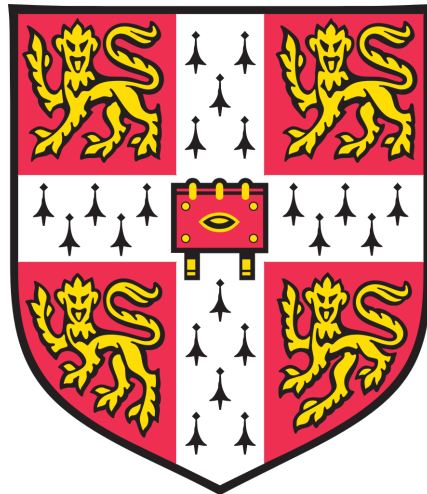


# Modelling the Electron Beam Welding of Nuclear Reactor Pressure Vessel Steel

Christopher J. Duffy

28 August, 2014

Supervised by Professor H.K.D.H. Bhadeshia FRS FEng FNAE



Phase Transformations and Complex Properties Research Group  
Department of Materials Science and Metallurgy  
University of Cambridge

## **Abstract**

Electron beam welding offers exciting economic and materials property gains in industrial fabrication of thick-section steel for critical components such as reactor pressure vessels. Electron beam weld tests performed by Rolls-Royce and The Welding Institute of SA 508 Grade 3 and SA 508 Grade 4N are theoretically modelled and physically examined to provide partial validation for the use of existing theory in modelling this process.

# Contents

<b>1</b>	<b>Authenticity and Acknowledgments</b>	<b>3</b>
<b>2</b>	<b>Introduction</b>	<b>3</b>
2.1	SA508 Steel Properties, Applications, and Welding . . . . .	3
2.2	Electron Beam Welding . . . . .	4
2.3	Microstructure . . . . .	4
2.4	Intent of the Project . . . . .	5
2.5	Summary of Findings . . . . .	5
<b>3</b>	<b>Literature Review</b>	<b>6</b>
3.1	TWI Reports . . . . .	6
3.2	Other Literature . . . . .	8
<b>4</b>	<b>Method</b>	<b>8</b>
4.1	Development of the Weld Cooling Curve . . . . .	8
4.2	mucg65: Weld Microstructure . . . . .	9
4.3	Physical Examination . . . . .	10
<b>5</b>	<b>Cooling Curve and Heat Input</b>	<b>10</b>
5.1	Development of the Cooling Curve . . . . .	10
5.2	Heat Input . . . . .	12
<b>6</b>	<b>Theoretical Microstructure Evolution of Electron Beam Welded SA508 Grade 3 and SA508 Type 4N Steel</b>	<b>12</b>
6.1	Phases . . . . .	12
6.2	Formation of $\delta$ -Ferrite and Austenite from the Weld Pool . . . . .	13
6.3	Transformation from Austenite to Ferrite . . . . .	14
6.4	The Formation of Ferritic Microstructure . . . . .	16
6.5	mucg65 Modelling Summary . . . . .	21
<b>7</b>	<b>Physical Examination of Weld Samples</b>	<b>22</b>
7.1	Metallographic Preparation . . . . .	22
7.2	Weld Cross-sections . . . . .	22
7.3	Parent Metal Samples . . . . .	29
<b>8</b>	<b>Conclusion of the Theoretical and Physical Results</b>	<b>32</b>

# 1 Authenticity and Acknowledgments

This dissertation is substantially my own work and conforms to the University of Cambridge’s guideline on plagiarism. Where reference has been made to other research this is acknowledged in the text and bibliography.

I would like to thank Professor Harry Bhadeshia for his guidance and consistently warm reception. Further, I would like to thank the members of his Phase Transformations and Complex Properties Research Group for their help and support, most especially Neelabhro Bhattacharya who never hesitated to offer his valuable time and understanding, but also Dr. Hector Pous-Romero, Dr. Matthew Peet, and Guo Lei. Aside from this academic support, I would like to thank those closest to me at this time who have provided much needed encouragement and, at times, diversions: my partner Freya Jephcott and my good friends Ben Folit-Weinberg and Daniel Peat.

This work would not be possible without the assistance of Rolls-Royce who graciously provided weld samples and internal reports. Dr. Luke Burling, Metallurgy Technologist, has been thoroughly supportive and kind.

## 2 Introduction

### 2.1 SA508 Steel Properties, Applications, and Welding

SA508 is a low-alloy steel commonly used in high pressure, high temperature structural components, such as nuclear reactor pressure vessels (RPVs). Different grades of SA508 are specified by ranges of composition. SA508 Grade 3 is particularly common in Pressurized Water Reactor (PWR) reactor pressure vessels due to its strength, toughness, weldability, and cost. SA508 Grade 4N is a further improvement upon the strength and toughness of SA508 Grade 3 brought about through an increase in nickel and chromium and decrease in manganese concentrations [17, 19]. The ASTM specification for SA508 Grade 3 and 4N compositions is given in Table 1.

Table 1: ASTM SA508 Specification Compositions, wt% [1, 19]

	Grade 3	Grade 4N
Carbon	$\leq 0.25$	$\leq 0.23$
Silicon	0.15 - 0.35	$\leq 0.30$
Manganese	1.20 - 1.50	0.20 - 0.40
Nickel	0.40 - 1.00	2.8 - 3.9
Molybdenum	0.45 - 0.60	0.40 - 0.60
Chromium	$\leq 0.25$	1.25 - 2.00
Vanadium	$\leq 0.05$	$\leq 0.03$

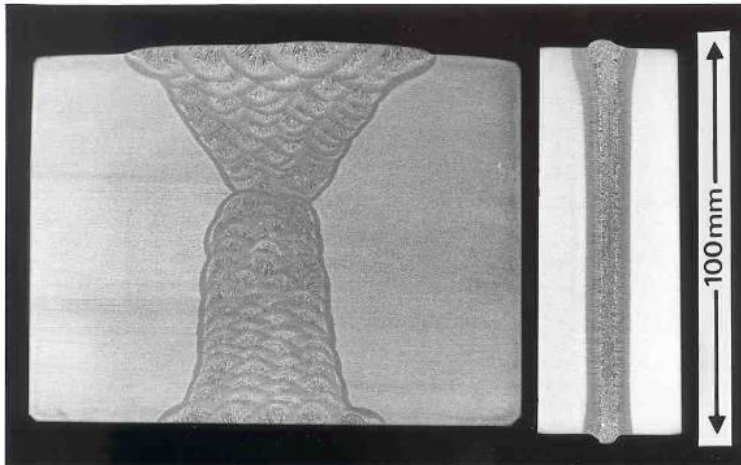
Such critical components are typically welded using an arc welding process

such as submerged arc welding. Due to their large size - particularly in the case of RPVs - welds are multi-pass and require a significant number of passes, e.g. on the high order of tens, to complete the weld. Further, an arc welding process requires a filler material. RPVs have not yet been welded with an electron beam (EB).

## 2.2 Electron Beam Welding

EB welding has several advantages over traditional arc welding in this case. The primary construction advantage is that EB welding can be single-pass and therefore take far less time to complete than a multipass weld. This time difference is significant, and can be best demonstrated by comparing an arc weld and an EB weld side by side as in Figure 1. The two main structural advantages are that the weld is autogenous - no filler metal is used - and that the weld is typically performed under vacuum, meaning that gas contaminants can be effectively eliminated from the weld. The autogenous EB weld performed under vacuum therefore leaves a nearly seamless weld that is of essentially the same composition as the parent metal, performed in a very small fraction of the time that would be required for traditional welding methods. EB welding, however, suffers from the difficulty of having to establish a vacuum which slows the preparation. Further, with respect to RPVs, EB welding has not yet met certification criteria to be used in manufacture.

Figure 1: Comparable multi-pass arc (left) and single-pass EB (right) welds [11]



## 2.3 Microstructure

The microstructure of a material describes the phases of a material, or the structure of the grain crystal lattices and precipitates within that material.

The microstructure often occurs at a very small scale, on the order nanometres to micrometres, though sometimes very large crystals can be of the order of millimetres or even decimetres. In steels, the microstructure is commonly between the orders of 100 nanometres to 100 micrometres. The phases form by various processes, but are understood well in terms of kinetics and thermodynamics. Phases grow and consume other phases as described by kinetics, and have energy levels and driving forces for transformation as described by thermodynamics. Welding is one such process where the microstructure of steel changes. Importantly, the microstructure of a material is a strong determinant of a material's properties. It is therefore useful to not only know the microstructure of the material used, but also the processes by which that microstructure forms so that it might be controlled when certain properties are desired.

## 2.4 Intent of the Project

The intent of the project is to examine a theoretical model for the formation of the as-deposited weld microstructure that results from the EB welding of thick-section SA508 steel. The theories used to examine this model are relatively long-standing kinetic and thermodynamic principles that have been informed by many decades of empirical work. Samples of such welds are then physically examined to determine to what extent the resulting microstructure resembles that developed by the established theory. Successfully modelling the as-deposited microstructure would lend confidence to the use of EB welding in joining the SA508 steel. Such success would then form part of a large safety case justifying the use of the SA508 steel joined by EB welding in critical components typical of SA508 steel applications, e.g. RPVs. In particular, this project examines the use of The Welding Institute (TWI) 150 kV Reduced Pressure Electron Beam (RPEB) gun in welding 140 mm and 147 mm thickness SA508 Grade 3 and SA508 Grade 4N sections, respectively. Rolls-Royce commissioned TWI to develop RPEB welding practices for such sections, and this work follows directly from the resulting TWI reports and samples of the welds provided by Rolls-Royce.

## 2.5 Summary of Findings

Temperature traces from RPEB welding are fitted with a cooling curve model, describing coefficients  $C_1$  and  $C_2$  that determine the cooling rate for RPEB welding of thick-section steel. The mucg65 model, using the fitted cooling curve, seems to underestimate the formation of martensite. This criticism is based on physical testing of weld samples of SA 508 steel from RPEB welding. Further testing will be necessary to ensure the accuracy of the cooling curve and the identification of the resulting physical microstructure, particularly the seemingly bainitic structures.

## 3 Literature Review

### 3.1 TWI Reports

The majority of the relevant literature comes from reports to Rolls-Royce from TWI regarding the EB weld tests on SA508 steel requested by Rolls-Royce. This exploration to develop EB welding methods occurred in two phases, the first phase investigated EB welding of SA508 Grade 3 steel and the second phase investigated EB welding of a composition of the newer SA508 Grade 4N steel. The EB welding performed was done with the TWI 150 kV RPEB gun, itself under development.

**RPEB Development** RPEB welding is an adaptation of earlier EB welding practices that is intended for use with a local, moving vacuum that travels over the component and weld. EB welding is otherwise performed with the whole workpiece within a vacuum chamber. Obviously, this is restrictive for large components such as RPVs. The RPEB welding method does not draw a high vacuum which would nominally be of the order  $10^{-3}$  mbar, but instead operates at around 1 mbar vacuum with gas shielding, on either a flat plate or with a joint and weld bead present. A moving, local vacuum would allow the speed benefits of EB welding to be fully realized in commercial applications [21].

**EB Welding Phase 1** The first phase of the project sought to develop suitable weld conditions for various thicknesses of SA508 Grade 3. Forgings of SA508 Grade 3 were provided to TWI by Rolls-Royce which were later tested and shown to have the compositions listed in Table 2. The large section compositions conform to the specification and are notably homogeneous.

Table 2: Phase 1 SA508 Grade 3 Composition, wt% [1, 19, 25]

	ASTM Specification	Forging					Average
		A	B1	C1	D1	E	
Carbon	$\leq 0.25$	0.16	0.17	0.18	0.16	0.18	0.17
Silicon	0.15 - 0.35	0.26	0.25	0.25	0.23	0.25	0.248
Manganese	1.20 - 1.50	1.37	1.37	1.42	1.36	1.39	1.382
Nickel	0.40 - 1.00	0.76	0.77	0.8	0.78	0.76	0.774
Molybdenum	0.45 - 0.60	0.56	0.52	0.52	0.49	0.51	0.52
Chromium	$\leq 0.25$	0.23	0.23	0.35	0.23	0.24	0.236
Vanadium	$\leq 0.05$	0.002	0.002	0.003	0.002	0.002	0.002

The forgings were each halved and butt welded back together. However, milling was performed along the seam to create different weld depths of 100 mm, 140 mm, 160 mm, and 180 mm on different test pieces. Also prior to welding, the sections underwent demagnetization to reduce the residual magnetism below

5 Gauss, which would otherwise deflect the electron beam and produce voids in the weld. The welds were not produced with a local, moving vacuum, but were instead performed in a large vacuum chamber using the RPEB gun with the vacuum between  $2 \times 10^{-2}$  mbar and  $8 \times 10^{-2}$  mbar with helium used as a gas shield [22].

The welding conditions for the sections with various depths were altered by adjusting the RPEB current and travel speed of the work piece, thus changing the linear heat input [22]. A summary of the developed conditions is given in Table 3. Due to the practical focus of the project, linear heat input was not of primary concern. However, it is an important determinant of the weld microstructure as it determines the cooling curve of the weld. Only an informal estimate of the beam efficiency was available from TWI, with an estimated 70% of the beam energy deposited in the weld [2]. The calculated linear beam output and estimated linear heat input are included in Table 3 as they will be used below to determine the cooling rates.

Table 3: Phase 1 Welding Conditions for Varied Depth Sections, [22]

	100 mm	140 mm	160 mm	180 mm
Voltage, kV	150	150	150	150
Current, mA	280	318	350	370
Welding Speed, mm/min	125	100	100	100
RPEB Output, kJ/mm	20.16	28.62	31.50	33.30
Linear Heat Input, kJ/mm	14.11	20.03	22.05	23.31

The resulting welds underwent a post-weld heat treatment (PWHT) typical for welds of this steel:  $607 \text{ }^\circ\text{C} \pm 13 \text{ }^\circ\text{C}$  in an air furnace for 3.5 h, and cooled at  $20 \text{ }^\circ\text{C}$  per hour to  $300 \text{ }^\circ\text{C}$  before still air cooling to ambient temperature [22]. A series of mechanical, chemical, and visual tests were performed on the resulting 100 mm and 160 mm welds including tensile, fracture toughness, and hardness [25]. Only the hardness testing is discussed, and is introduced below in comparison with hardness tests performed by the author on weld samples that did not undergo the PWHT.

**EB Welding Phase 2** The second phase of the project intended to develop suitable weld conditions for various thicknesses of SA508 Grade 4N. However, due to complications arising from strongly magnetic forgings, the focus of the second phase became to develop effective demagnetizing procedures for SA508 Grade 4N forgings such that they might be suitably welded using the RPEB process. Forgings of SA508 Grade 4N were provided to TWI by Rolls-Royce, and four demagnetization methods carried out. Three of those demagnetization methods were performed by TWI and were insufficient. The final and successful method was a switched DC demagnetizing method performed by a company called DCNS located in Brittany [23]. Chemical composition of the parent

metal was taken from only one sample is and recorded in Table 4. Similarly, the forged SA508 Grade 4N falls within the specifications.

Table 4: Phase 2 SA508 Grade 4N Composition, wt% [1, 19, 25]

	ASTM Specification	Forging
Carbon	$\leq 0.23$	0.22
Silicon	$\leq 0.30$	0.05
Manganese	0.20 - 0.40	0.05
Nickel	2.8 - 3.9	3.69
Molybdenum	0.40 - 0.60	0.56
Chromium	1.25 - 2.00	1.92
Vanadium	$\leq 0.03$	0.002

As in the first phase, the forgings were halved, and the successfully demagnetized sections were butt welded back together. Milling was performed along the seam to create a weld depth of 147 mm. The weld conditions were the same as those for the 140 mm weld of phase one shown in Table 3, including the use of the stationary RPEB gun mounted onto the vacuum chamber and simulating the RPEB vacuum and shield gas conditions [23]. The successful weld also underwent a PWHT as that for the welds in phase one, though at a lesser temperature for much longer:  $565\text{ }^{\circ}\text{C} \pm 14\text{ }^{\circ}\text{C}$  in an air furnace for 30 h. A cooling rate was not specified [26]. The same series of mechanical, chemical, and visual tests were performed on the resulting 147 mm weld with a PWHT as in phase 1 [25]. Again, only the hardness testing is discussed, and is introduced below in comparison with hardness tests performed by the author on a weld sample that did not undergo the PWHT.

### 3.2 Other Literature

There are other relevant papers to introduce, but as they are all theoretical and apply directly to the model, they are better discussed below in the section on the theoretical microstructure development.

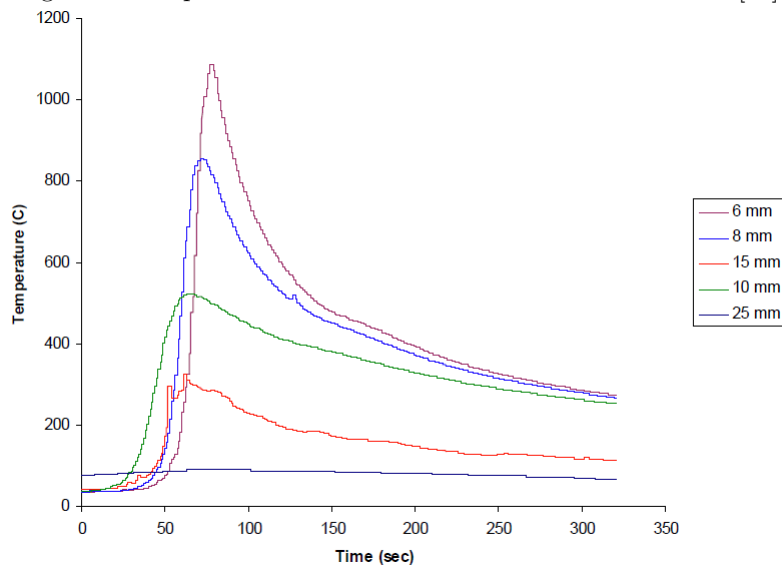
## 4 Method

### 4.1 Development of the Weld Cooling Curve

During the first phase of the RPEB weld method development at TWI, temperature traces were taken on one of the welds performed on a 160 mm thickness milled section, shown in Figure 2. The traces were taken with thermocouples mounted on the root side of the weld at 6 mm, 8 mm, 10 mm, 15 mm, and 25 mm from the weld centreline. The thermocouples were not placed along a perpendicular line, but rather were staggered with 10 mm spacing [22]. This

spacing should account for some of the time difference in the trace peaks. Unfortunately, since weld cooling rates were not of interest at the time of the testing, no other temperature traces were taken or available, and the data for the trace taken were not saved aside from the trace image itself. However, the trace data in this image are ostensibly more likely to be characteristic of further welds of this kind than data from other EB welds of other materials. Hence, the development of the cooling curve uses these trace image data and the heat input data discussed above. Cooling coefficients of a form described below are then used to drive a cooling curve model.

Figure 2: Temperature traces from 160 mm Phase 1 EB weld [11]



## 4.2 mucg65: Weld Microstructure

A number of steel weld microstructure prediction software models have been developed by Professor H.K.D.H. Bhadeshia of the University of Cambridge Department of Materials Science and Metallurgy. These models have the prefix mucg, and are built from subroutines publicly hosted by Professor Bhadeshia's Phase Transformations and Complex Properties Research Group and the National Physical Laboratory on the Materials Algorithms Project website [18]. The subroutines themselves are a collection of theoretical relationships based on kinetic theory and thermodynamics. The model used in this project is a commercially sensitive construction of these subroutines named mucg65. The mucg65 program uses the chemical composition of the parent metal, the cooling curve of the weld, and the austenite grain size - a sufficient measure of the initial geometry - to calculate the formation and transformation of various phases in

the weld metal. Thus, the mucg65 model is used to demonstrate the theoretical evolution of the weld microstructure and resulting as-deposited microstructure.

### 4.3 Physical Examination

Samples of EB welds provided by Rolls-Royce are physically examined by hardness testing and optical microscopy. One 140 mm sample from Phase 1 (SA 508 Grade 3) and one 147 mm sample from Phase 2 (SA508 Grade 4N) of the TWI testing are used. Neither underwent a PWHT and were received in the as-welded condition, necessary in order to examine the as-deposited microstructure.

Hardness traverses are performed with a diamond pyramid indenter across the welds to characterize the hardness of the heat affected zone (HAZ) and the weld metal, but also to use the hardness data to aide in differentiating between the potential microstructures present. Optical micrographs are taken of the welds to measure the prior austenite grain size - an input to the mucg65 model - and to examine the microstructure and determine the presence of various phases.

Making a determination of the as-deposited weld microstructure can be difficult to do for some phases, such as those found in this weld metal. To further aide in discriminating the phases present, parent metal was removed from the two weld samples and heat treated to form a phase called martensite with certainty. This martensitic steel was then hardness tested so that comparisons could be made to the hardness data taken from the weld and HAZ of both samples.

## 5 Cooling Curve and Heat Input

### 5.1 Development of the Cooling Curve

The tabulated data were not available for the thermocouple traces, so the trace image was first digitized using a freeware program called GetData [12]. It was then desired to develop coefficients  $C_1$  and  $C_2$  for equation 1.

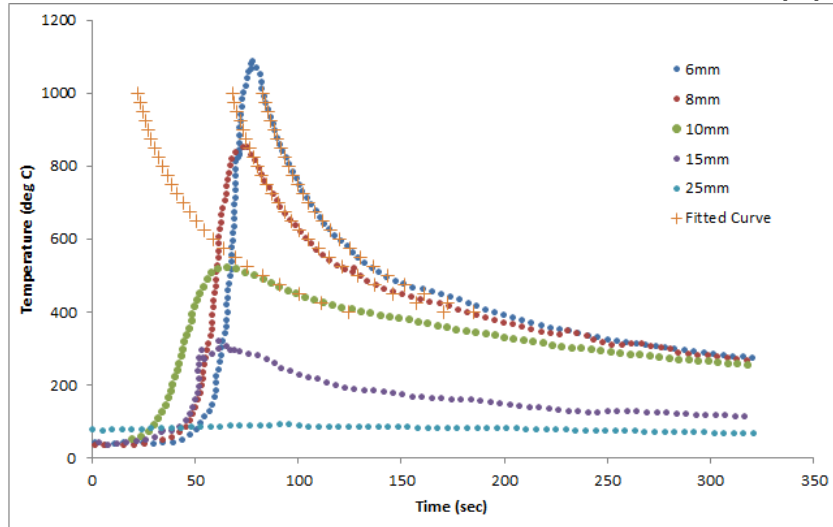
$$Time(I) = \frac{Q\eta (T_{high} - T_{int})^{1-C_2} - (T(I) - T_{int})^{1-C_2}}{v C_1(1 - C_2)} \quad (1)$$

Equation 1 is a modified form of equation 1c given in [16] that is used in the mucg65 model to develop the cooling curve. Time(I) is the time that it takes to reach temperature T(I) from temperature  $T_{high}$  with interpass temperature  $T_{int}$ .  $Q$  is the heat output of the beam or arc in Watts,  $\eta$  is the efficiency of the beam or arc, and  $v$  is the travel speed in metres per second. The cooling rate used by the mucg65 model is also modified from equation 1b in [16], shown as equation 2.

$$\frac{dT}{dt} = C_1 \frac{v}{Q\eta} (T - T_{int})^{C_2} \quad (2)$$

In order to fit  $C_1$  and  $C_2$ , equation 1 was overlaid on top of the digitized thermocouple traces shown in Figure 3, using weld conditions for the 160 mm weld shown in Table 3. The value for  $\eta$  used was 0.7 according to [2]. The mucg65 model begins examining cooling times at a  $T_{high}$  of 1000 °C, and the interpass temperature  $T_{int}$  for a single-pass weld is assumed to be ambient at 25 °C. Values for equation 1 were generated at 25 °C intervals down to 400 °C. Initial values of  $C_1$  and  $C_2$  were set to those from previous modeling in mucg65 of laser welds: 498.42 and 2.05, respectively. The time index was shifted for equation 1 such that the mark at 1000 °C coincided with the mark for the 6 mm trace. A visual fit to the 6 mm trace was then performed using  $C_1$  as the primary adjustment and  $C_2$  as the secondary adjustment.  $C_1$  was therefore incrementally adjusted and  $C_2$  corrected to return the curve to the 6 mm trace. This iterative process found that the concavity best visually matched the 6 mm curve with a  $C_1$  of 5 and subsequent  $C_2$  value of 2.66, though the fit begins to fail below 500 °C. Interestingly, having fit equation 1 to the 6 mm curve, and then shifting the time index such that equation 1 then overlaid the 8 mm and subsequently the 10 mm curves, it was found that the coefficients  $C_1$  and  $C_2$  also fit these traces fairly well. It is then a plausible extrapolation to say that the weld metal - which lies within a distance of approximately 4 mm from the weld centre on both sides, once in the temperature range 1000 °C to 500 °C, also cools according to the fitted equation 1.

Figure 3: Digitized Thermocouple Traces and Fitted Equation 1 [11]



Ideally, many thermocouple traces would be taken over a large number of tests, including traces from the weld centre after the beam has passed, and the coefficients  $C_1$  and  $C_2$  would be averaged over the aggregate data as was done in [16]. However, the fit given should be sufficient for the modeling purposes

here.

## 5.2 Heat Input

If equation 1 is as good a model for thick-section RPEB welds as it has been for a large variety of other welds [13], the fitted coefficients  $C_1$  and  $C_2$  can be considered characteristic of RPEB welding of thick-section steel. These coefficients can therefore be used to determine the theoretical cooling rates in the 140 mm SA508 Grade 3 and 147 mm SA508 Grade 4N weld centres using the data in Table 3, or for other thick-section steel under other, similar welding conditions.

# 6 Theoretical Microstructure Evolution of Electron Beam Welded SA508 Grade 3 and SA508 Type 4N Steel

## 6.1 Phases

The modelling of the evolution of steel weld microstructure has been improving over many decades. However, the transformations can be essentially understood in terms of kinetic theory and thermodynamics. In the process of welding, the weld metal is melted as the arc or beam passes over it, and then solidifies and cools following the pass. The cooling of the weld and the compositions of the weld metal, parent metal, and gas present determine the resulting microstructure transformations during solidification and cooling to ambient temperature.

The phases of interest in this project are those of the primary microstructure, principally a body-centred cubic phase called ferrite and a face-centred cubic phase called austenite. Other phases are possible, but are not thermodynamically stable in the SA 508 Grade 3 and SA508 Grade 4N steels in significant populations. This can be seen in Figure 4 which shows the thermodynamically stable phases with mass fractions reaching at least one percent in SA508 Grade 3 (left) and SA508 Grade 4N (right) with compositions given in Tables 2 (Average) and 4, respectively. These graphs were generated using a thermodynamics database and modelling program called MTDATA, using the plus, sub\_sgte, and sgte\_sol databases [24]. Small regions of solute depleted or enriched material left behind after the formation of the primary microstructure, termed microphases, are likely to form also but are not under consideration here.

The two diagrams of Figure 4 can be compared to note the differences in stability of austenite. Austenite is stable above an Ae3 temperature of 800 °C in SA508 Grade 3 and 760 °C in SA508 Grade 4N, and becomes completely unstable below an Ae1 temperature of 660 °C in SA508 Grade 3 and 620 °C in SA508 Grade 4N, summarized in Table 5. The temperatures are approximate due to a 20 °C resolution. The austenite is stable at lower temperatures in the SA 508 Grade 4N which has a significantly higher nickel content. This fits with the common notion of nickel as an austenite stabilizer.

Figure 4: Thermodynamically Stable Phases in SA508 Grade 3 (left) and SA508 Grade 4N (right) [24]

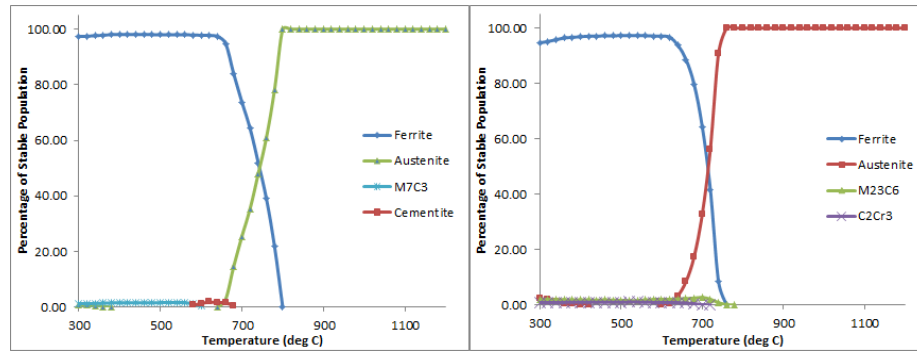


Table 5: Approximate Equilibrium Austenite Stability Temperatures in °C for SA508 Steel [24]

	Ae1	Ae3
SA 508 Grade 3	660	800
SA 508 Grade 4N	620	760

## 6.2 Formation of $\delta$ -Ferrite and Austenite from the Weld Pool

After the electron beam passes and the liquid weld metal starts to cool, columnar  $\delta$ -ferrite grains are nucleated on the equi-axed  $\delta$ -ferrite grains at the fusion boundary, and begin to grow towards the weld centre. ( $\delta$ -ferrite and  $\alpha$ -ferrite are identical, but the name  $\delta$ -ferrite is given to ferrite stable at high temperatures between austenite and liquid phase regions, and  $\alpha$ -ferrite at lower temperatures, below the austenite phase region.) These columnar grains are not nucleated on the same plane, and thus grow in different directions and compete. The columnar grains oriented in the direction of the heat flow grow fastest and thus win out over grains less aligned with the heat flow. These columnar grains can be approximated as an array of high aspect-ratio hexagonal prisms [9].

As the weld metal solidified as  $\delta$ -ferrite cools further, austenite becomes thermodynamically stable and preferential to ferrite, and austenite grains nucleate at the boundaries between the columnar  $\delta$ -ferrite grains, replacing the  $\alpha$ -ferrite entirely with a similar array of hexagonal prisms. Cooled still further,  $\alpha$ -ferrite becomes thermodynamically stable and preferential, with many important mechanism for growth, described below. The size of the austenite grains is of importance for the phase transformation to  $\alpha$ -ferrite for two main reasons: the size is a proxy for the grain surface area per unit volume and therefore

the nucleation site density, and the size determines the time for a particular structure of ferrite to grow across the inside of an austenite grain [9]. Thus, the austenite grain size is an important input to the mucg65 model. Since the determinants of austenite grain size are not well enough understood to support a theoretical size evaluation, it can only be either measured physically by examining a metallographically prepared section of the weld, or by estimating using an empirical formula [10]. An empirical formula is available in [10], but the welds under consideration fall well outside the data used in that regression analysis [16]. Austenite grain size measurements were physically measured for both steel weld samples, as described in detail below, and input into the mucg65 model.

### 6.3 Transformation from Austenite to Ferrite

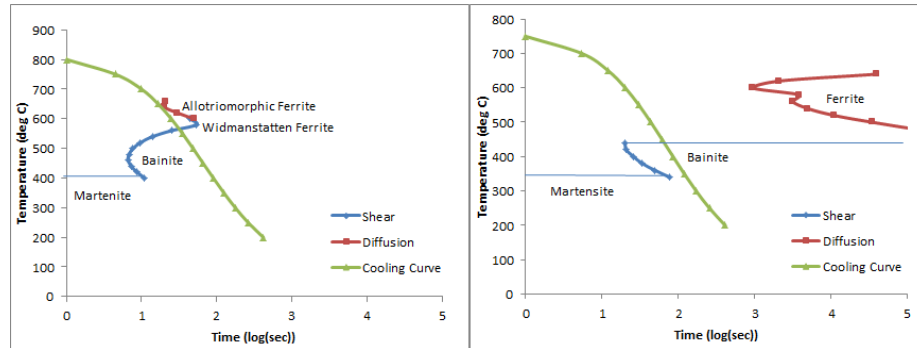
The phase transformation that takes place from the hexagonal columnar austenite to  $\alpha$ -ferrite in steel welds is much more complex and more important than the earlier transformations to  $\delta$ -ferrite and austenite. It is more complex because there are many potential mechanisms for the transformation and resulting structures of ferrite. It is more important because the ultimate microstructure will be ferritic for these steels, and the properties will depend on the process-dependent structures formed. The dominant structures formed in the SA508 welds considered are theoretically bainite and martensite, though allotriomorphic ferrite and Widmanstätten ferrite also theoretically form in the SA508 Grade 3 weld.

The mucg65 model treats each of these processes separately; the theory of formation for each is given below along with the results of that theory applied to the SA 508 Grade 3 and SA 508 Grade 4N RPEB welds.

**Time-Temperature-Transformation Diagrams and Cooling Rates** It will be useful to jump ahead to some of the results of the model so that the following sections on the development of the ferritic microstructures can be seen in context. In the model, the cooling rate of equation 2 and cooling time of equation 1 are used with coefficients  $C_1$  and  $C_2$  fitted to a particular welding process in order to develop a cooling curve such as that shown imposed upon the thermocouple traces in Figure 3. In addition, based on thermodynamics, nucleation, and kinetics, a pair of c-curves are developed, so called for their shape. One curve describes the incubation time for diffusive transformations to occur, the other for displacive or shear transformations to occur. These c-curves can be displayed as a time-temperature-transformation diagram (TTT) as in Figure 5, and overlaid with a cooling curve, can provide an indication of the resulting microstructure as the material cools between the regimes of the different transformations. Figure 5 is a part of the result of the mucg65 model for the SA508 Grade 3 and SA508 Grade 4N steels. If the two diagrams are compared, it can be seen that SA508 Grade 4N would require a slower cooling rate than SA508 Grade 3 in order to undergo diffusive transformations to allotriomorphic ferrite and pearlite. Similarly, for the cooling curves given, the SA 508 Grade 4N should surely be a mixture of martensite and bainite,

and the SA508 Grade 3 mostly a mixture of martensite and bainite, but also including some allotriomorphic ferrite and Widmanstätten ferrite. This is in fact the result given by the mucg65 model, explained in detail below.

Figure 5: TTT Diagrams of SA508 Grade 3 (left) and SA508 Grade 4N (right) Steels with Theoretical RPEB Cooling Rate [13]



Diffusive transformations are those in which the lattice is reconstructed to form the new phase, requiring the diffusion of atoms to and from the new phase to meet the correct composition. For example, the solubility of carbon in austenite is greater than the solubility of carbon in ferrite. In order for a ferrite structure to form by a diffusive or reconstructive transformation from carbon-saturated austenite, carbon will have to be rejected from the product ferrite and diffuse into the bulk of the austenite [9]. Such is the case for the only diffusive transformation under consideration in this paper, that of the transformation to allotriomorphic ferrite. Kinetics therefore play a large role in the formation of allotriomorphic ferrite. The resulting incubation times for allotriomorphic ferrite and diffusive transformations take the form of a ‘c’ and are called c-curves for the following two reasons: the further below the temperature  $Ae_1$  where austenite is unstable and ferrite is preferred, the greater the driving force for transformation, but the diffusion of atoms requires thermal energy and therefore diffusion slows with decreasing temperature. Thus, there is an optimum temperature for the transformation to allotriomorphic ferrite, the point at which the transformation requires the least incubation time: the nose of the c-curve. Above the nose of the c-curve, the thermodynamic driving force for transformation diminishes too rapidly, and below the thermal energy available for diffusion diminishes too rapidly for the optimum conditions [9].

Displacive transformations are those in which no diffusion occurs; the product phase results from a strain that shapes the lattice into the product. The strain energy typically comes from a large thermodynamic driving force, as in the rapid cooling, or quenching, of a material. In the cooling of steel welds, Widmanstätten ferrite, bainite, and martensite are ferritic structures that occur by displacive, shear transformations [9].

To be clear, though, most transformations are a combination of shear and diffusion. They are grouped as above by the dominant mechanism. For example, bainite and Widmanstätten ferrite continue to form at a given temperature, requiring thermal energy in the diffusion of atoms [9].

## 6.4 The Formation of Ferritic Microstructure

**Allotriomorphic Ferrite** Allotriomorphic ferrite is ferrite that nucleates at the austenite grain boundaries and grows by diffusion. It wets the grain boundaries and forms continuous grains easily because diffusion is more likely along the grain boundaries. Once nucleated, the allotriomorphic ferrite displays parabolic growth. The reason for parabolic growth is that the newly formed ferrite must partition carbon into the austenite due to its lower interstitial solubility. The rejection of carbon into austenite from the ferrite increases the concentration of the carbon in the austenite, thus reducing the free energy gradient between the two, slowing the diffusion of carbon out of the ferrite, and thus slowing the growth of the ferrite. Ferrite also has a lower solubility for substitutional solutes, though under common circumstances it is difficult for the substitutional solutes, which are much larger, to diffuse. Thus, the growth of allotriomorphic ferrite is considered under paraequilibrium conditions, with the concentrations of the substitutional solutes treated as fixed, yet allowing for carbon diffusion [9].

The growth of allotriomorphic ferrite can be described by a parabolic thickening rate constant  $\alpha_1$  which gives a half-thickness  $q = \alpha_1 t^{\frac{1}{2}}$ , where  $\alpha_1$  can be solved by equating the chemical potential of carbon in the ferrite and austenite, under the paraequilibrium conditions described, as shown in equation 3, where  $x^{\alpha\gamma}$ ,  $x^{\gamma\alpha}$ ,  $\bar{x}$ , and  $\bar{D}$  are the paraequilibrium concentrations of carbon in ferrite and austenite (austenite is typically denoted as  $\gamma$ ), the bulk carbon concentration in the austenite, and the weighted average diffusivity of carbon in austenite [10].

$$\frac{x^{\gamma\alpha} - \bar{x}}{x^{\gamma\alpha} - x^{\alpha\gamma}} = \sqrt{\frac{\pi}{4\bar{D}}} \exp\left(\frac{\alpha_1^2}{4\bar{D}}\right) \operatorname{erfc}\left(\frac{\alpha_1}{2\bar{D}^{\frac{1}{2}}}\right) \quad (3)$$

The half-thickness  $q$  can be integrated over a period of time  $t_\alpha$  equivalent to the time taken for the cooling curve to pass from  $T_h$  to  $T_l$  in order to achieve the thickness of the allotriomorphic ferrite layer. The temperature at which the transformation begins  $T_h$  can be calculated using the TTT diagram and cooling curve generated and shown in Figure 5, adjusting the approach of the cooling curve to the c-curve using Scheil's additive rule to account for continuous cooling. The temperature at which the transformation ends is set to the intersection of the shear and diffusive c-curves, where displacive transformations become favored. From the calculated half-thickness  $q$  the volume fraction of allotriomorphic ferrite  $v_\alpha$  formed during the cooling of the weld can be calculated using the geometry of the hexagonal prism array of the original austenite in which the allotriomorphic ferrite grows. [10]. Unfortunately, though this theory empirically accounts for a very high percentage of the variation in allotriomorphic volume fractions, a correction factor is necessary [14]. The mucg65 model,

on these principles, calculates the results summarized in Table 6 for the RPEB weld of SA 508 Grade 3. As indicated in Figure 5, allotriomorphic ferrite does not form in the SA 508 Grade 4N with the welding conditions considered.

Table 6: Theoretical Formation of Allotriomorphic Ferrite in RPEB welded SA 508 Grade 3 Steel [13]

	$T_h$	$T_l$	$t_\alpha$	$q$	$v_\alpha$
SA 508 Grade 3	703 °C	607 °C	13.78 s	6.98 $\mu\text{m}$	0.0873

From Table 6 it can be seen that a relatively small fraction of allotriomorphic ferrite forms in the SA508 Grade 3 weld metal. This is due to the cooling curve barely entering the diffusive  $c$ -curve shown in Figure 5, after accounting for the Scheil additive rule for continuous cooling. The resulting thickness of the theoretical allotriomorphic ferrite along the prior austenite grain boundaries is thus quite small, forming  $7\mu\text{m}$  coatings on hexagonal grains that are on average  $362\mu\text{m}$  across.

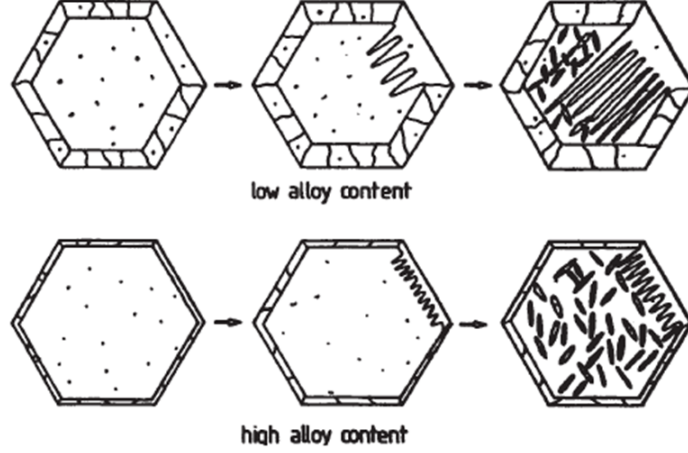
**Widmanstätten Ferrite and Acicular Ferrite** Widmanstätten ferrite is a ferritic structure that occurs by a shear transformation, nucleating either from the austenite grain boundary as in primary Widmanstätten ferrite, or from the allotriomorphic ferrite after it has coated the austenite grain boundary, as in secondary Widmanstätten ferrite. The process is diffusionless, though carbon does partition from the ferrite into the austenite. It is able to do so because it grows in plates that lengthen at the tip, thus encountering 'fresh' austenite which has not yet received partitioned carbon from the growth of ferrite. As a result, Widmanstätten ferrite does not show parabolic growth as allotriomorphic ferrite does, and is able to grow quite quickly relative to the time scale of the weld cooling. However, the growth of Widmanstätten ferrite is competitive with acicular ferrite. The two must therefore be considered together [9]. Because Widmanstätten ferrite is formed by a shear transformation, its growth must account for a shear strain, typically about 50 J/mol, a relatively small amount [10].

Acicular Ferrite nucleates on non-metallic inclusions, or oxide lattice impurities, in the austenite grain. It is structurally similar or perhaps identical to bainite, described below, though this difference has not been fully resolved to date. The two are thought to be the same, but just nucleated in different manners. Acicular ferrite is not actually needle shaped, as its name suggests, but rather forms as thin, lenticular plates [10]. The growth of acicular ferrite is the same as that for bainite, and will be described in the section on bainite.

The competition of growth between Widmanstätten ferrite and acicular ferrite is shown schematically in Figure 6. In the low alloy content steel on the top row, there are fewer inclusions to nucleate acicular ferrite, thus Widmanstätten ferrite is able to grow across the grain essentially unimpeded. In the high alloy

content steel there is a greater density of inclusions for acicular ferrite nucleation, and the acicular ferrite thus formed impedes the growth of the Widmanstätten ferrite [9].

Figure 6: Competitive Growth of Widmanstätten Ferrite and Acicular Ferrite [9]



Widmanstätten ferrite is assumed to grow directly following the growth of allotriomorphic ferrite at temperature  $T_l$ . Its growth is given by equation 4 [10, 14, 18].  $C_4$  is a coefficient independent of alloy composition,  $G$  is the lengthening rate estimated using the theory of diffusion-controlled growth of parabolic cylinders [10, 18],  $L$  is a dimension describing the width of the hexagonal austenite prism,  $q'$  is an adjustment for the thickness of the allotriomorphic ferrite layer given in 6, and  $t_2$  is the time available for the Widmanstätten ferrite plates to grow across the austenite grain.  $t_2$  is then either equal to the time taken for such a plate to grow, or if acicular ferrite forms, it is equal to the critical time  $t_c$  when the plates become hindered by the growing acicular ferrite [10, 14, 18]. Though equation 4 is written largely in terms of the geometry of the austenite grain,  $v_w$  shows poor correlation with the growth rate  $G$ . This is due to the impingement of the Widmanstätten ferrite upon the acicular ferrite. Thus, the time  $t_2$  largely determines  $v_w$  if impingement occurs at all, and is controlled by the delay between the cessation of growth of the allotriomorphic ferrite and the onset of growth of the acicular ferrite [10].

$$v_w = C_4 G (L - 4q' \tan(30)) \frac{t_2^2}{L^2} \quad (4)$$

Since the theory supporting the nucleation and growth of acicular ferrite is not understood well enough for prediction of its volume fraction on first principles, the volume of acicular ferrite formed is set to equal the remaining volume after the formation of allotriomorphic ferrite and Widmanstätten ferrite. This

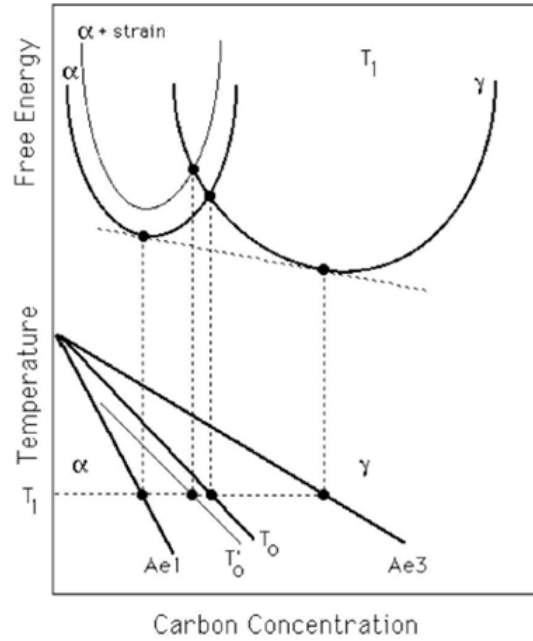
is typically sufficient if bainite and martensite do not form, though they do in both the SA 508 Grade 3 and SA 508 Grade 4N RPEB welds so this estimation is inaccurate. As for allotriomorphic ferrite, Widmanstätten ferrite only theoretically forms in the SA 508 Grade 3 weld, and  $v_w$  is calculated using equation 4 in mucg65 as 0.0057: essentially no Widmanstätten ferrite forms [13].

**Bainite** The bainite reaction occurs between the low temperature martensite and relatively higher temperature pearlite reactions. In the bainite reaction very small plates of ferrite form in sheaf-like aggregates, with carbides, particularly cementite ( $\text{Fe}_3\text{C}$ ), forming in between the plates. The ferrite plates are formed by a shear transformation which is accommodated in the austenite by plastic deformation. The associated strain energy in this transformation is measured to be around 400 J/mol, and the plastic deformation of the austenite accounts for the small size of each plate, which are each stifled by the deformation that occurs. New ferrite plates then nucleate at the end of the previous plate, the process continuing to build sheaves of such ferrite plates. Further, there is no diffusion during the formation of the bainitic plates, but the carbon does diffuse from the ferrite following the transformation. The extent to which the carbon escapes the ferrite plates differentiates between the two main types of bainite: upper bainite and lower bainite. Upper bainite forms at a higher temperature, and thus has enough thermal energy for the full diffusion of carbon from the ferrite plates and precipitation between the plates as cementite or other carbides. Lower bainite forms at a lower temperature and therefore not all of the carbon escapes the ferrite plate, but rather forms even smaller precipitates within the lower bainite plates in addition to a reduced amount of carbides between the plates [9].

The growth of bainite is modelled as an incomplete reaction from austenite to ferrite. This can be presented on a phase diagram with a  $T_0$  curve which gives the carbon concentration at which the austenite and ferrite free energy curves intersect for a given temperature, shown in Figure 7. The  $T_0$  curve is then shifted to account for the extra strain energy required in the bainite reaction, labeled  $T'_0$ . The equilibrium carbon concentrations in the austenite and ferrite are given by a parallel tangent construction upon the free energy curves of austenite and ferrite. Initially the plates grow from austenite with the bulk concentration of carbon. However, the carbon from the initial plates diffuses into the austenite and the next set of plates has to grow from carbon enriched austenite. This process continues until the austenite is enriched to the point of the  $T'_0$  curve, and will go no further, thus the reaction is termed incomplete [8, 9].

The reaction is modelled in mucg65 by determining the  $c$ -curve for the given composition, calculating the  $T_0$  and  $T'_0$  curves from thermodynamic data and the parallel tangent construction, and the bainite start temperature  $B_s$  above which bainite cannot form.  $B_s$  is calculated based on the point where the driving force for shear transformation exceeds the stored strain energy in bainite, assumed to be 400 J/mol [18]. The carbon concentration of the bainitic ferrite is given by [5] and the resulting volume of bainite formed is calculated by using the

Figure 7: Schematic Representation of  $T_0$  and  $T'_0$  Construction on a Paraequilibrium Diagram [8]



lever rule with the  $T_0$  and  $T'_0$  curves. The total volume of bainite formed is calculated by using the cooling curve and Scheil's additive rule integrating the bainite formed between the bainite start temperature  $B_s$  and the martensite start temperature  $M_s$ , above which the martensite reaction cannot occur [18]. Using this process, the mucg65 model calculates the results summarized in Table 7. Due to the unresolved understanding of the differences between bainite and acicular ferrite, the results are offered with reservation [13].

Table 7: Theoretical Formation of Bainite in RPEB Welded SA 508 Grade 3 and SA 508 Grade 4N Steel [13]

	$B_s$	$v_B$
SA 508 Grade 3	531 °C	0.66
SA 508 Grade 4N	440 °C	0.54

The SA 508 Grade 3 has a theoretically greater fraction of bainite than the SA 508 Grade 4N, in part due to the higher bainite start temperature in the SA 508 Grade 3.

**Martensite** The martensite reaction is similar to the bainite reaction in that it results from an invariant plane strain and is thus formed in shear. There is also an accompanying stored strain energy with that transformation. However, martensite forms much larger structures, that also take the shape of plates, but the martensite is either slipped or twinned in order to accommodate the transformation occurring within a fixed macroscopic shape. Further, the martensite transformation is athermal, meaning that the extent of the reaction is entirely independent of diffusion and dependent solely on the degree of undercooling below the martensite start temperature  $M_s$ , with the reaction completing at the martensite stop temperature [9]. Since the transformation rate is incredibly fast - as fast as the speed of sound within the steel - the transformation rate is not limiting, and the reaction can be modeled with just the martensite start and stop temperatures, the volume available for the martensite reaction at  $M_s$ , and the cooling rate. Such a relationship is given in equation 5 developed by Koistinen and Marburger [8]. The volume fraction of martensite can also be calculated using the Khan and Bhadeshia method described in [15,18]

$$v_M = 1 - \exp(\beta(M_s - T)) \quad (5)$$

The martensite start temperature is calculated as the temperature at which the available free energy accompanying the transformation from austenite to ferrite reaches the energy required for the martensite nucleation, somewhere between 900 and 1400 J/mol [3, 4, 18]. Using these relationships, the mucg65 model gives martensite results as shown in Table 8.

Table 8: Theoretical Formation of Martensite in RPEB Welded SA 508 Grade 3 and SA 508 Grade 4N Steel [13]

		Koistinen and Marburger	Khan and Bhadeshia
	$M_s$	$v_M$	$v_M$
SA 508 Grade 3	407 °C	0.20	0.15
SA 508 Grade 4N	347 °C	0.41	0.30

## 6.5 mucg65 Modelling Summary

The summary of input to the mucg65 model is given in Table 12 and the summary results of the model are given in Table 9. With the same welding conditions, these two SA 508 steels produced microstructures that have significant differences. The SA 508 Grade 4N steel with an expected higher hardenability due to the nickel content, has a 21% greater fraction of martensite than the SA 508 Grade 3, which should and does yield a significantly higher hardness in the as-welded samples, shown below. Also, the cooling curve for the SA 508 Grade 3 was very close to causing further diffusive transformations, which would have

been achieved with a slower cooling rate. Nearly 10% of the SA 508 Grade 3 is allotriomorphic ferrite. If allotriomorphic ferrite is present it can have important effects on the fracture toughness of the steel as cracks can form and propagate relatively easy along the large grains. Both welds showed a residual austenite fraction of 5%.

Table 9: mucg65 Model Output Summary [13]

	$v_\alpha$	$B_s$	$v_B$	$M_s$	$v_M$	$v_\gamma$
SA 508 Grade 3	0.09	531 °C	0.66	407 °C	0.20	0.05
SA 508 Grade 4N	0	440 °C	0.54	347 °C	0.41	0.05

## 7 Physical Examination of Weld Samples

A total of 13 samples were cut from the 2 weld sections. 3 of these samples were weld cross-sections that underwent metallographic preparation, hardness traverses, austenite grain measurements, and optical microscopy. The remaining 10 samples were sections of the parent metal - 5 from each sample - that were given a heat treatment (austenitize and quench) followed by metallographic preparation, hardness testing, and optical microscopy.

### 7.1 Metallographic Preparation

All samples metallographically prepared were done so by hand grinding on rotary machines with a progressive grit up to 2500, then hand polished on rotary machines with a 6  $\mu\text{m}$  then 1  $\mu\text{m}$  diamond paste before being etched with 2% Nital to reveal the grain structure.

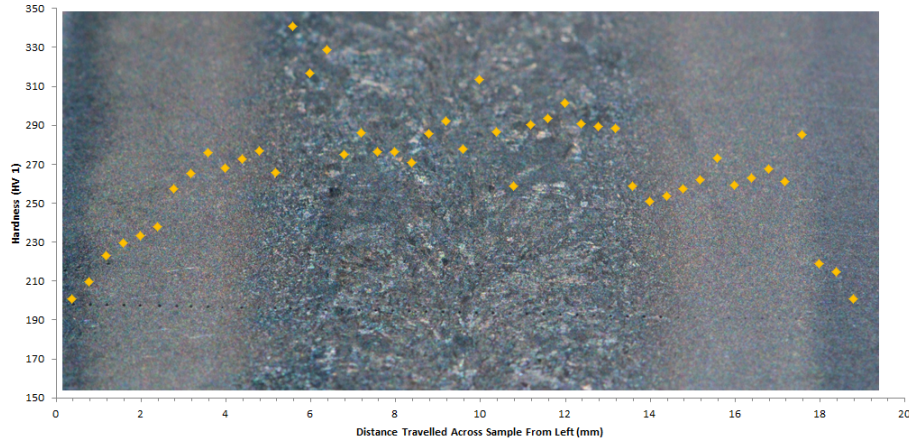
### 7.2 Weld Cross-sections

**Weld Hardness Traverses** Hardness traverses were performed across 2 of the 3 weld cross-sections samples, both being transverse sections, one from the SA 508 Grade 3 and one from the SA 508 Grade 4N weld. The SA 508 Grade 4N weld hardness traverse was performed twice to verify the initial results. The hardness testing was performed using a diamond pyramid indenter with a 1 kg load, except where a 300 g load was used for a portion of the initial SA 508 Grade 4N traverse. The indentations were performed at 400  $\mu\text{m}$  intervals, beginning and ending in the parent metal on either side of the weld. Distance measurements were taken using the mounting two-axis micrometres.

The hardness data for the SA 508 Grade 3 sample are overlaid on a photograph of the weld cross-section in Figure 8. This was done so that the hardness can be directly compared to the visible regions of the weld. The weld metal was approximately 10 mm across, with approximately 2.4 mm heat-affected zones

(HAZ) bands on either side of the weld metal. The hardness extends from approximately 195 HV in the parent metal, rising across the HAZ, to approximately 290 HV across the weld metal, with some modest fluctuations. The maximum hardness recorded was 340 HV.

Figure 8: Vickers Hardness Traverse of the SA-508 Grade 3 Weld without PWHT Cross-section

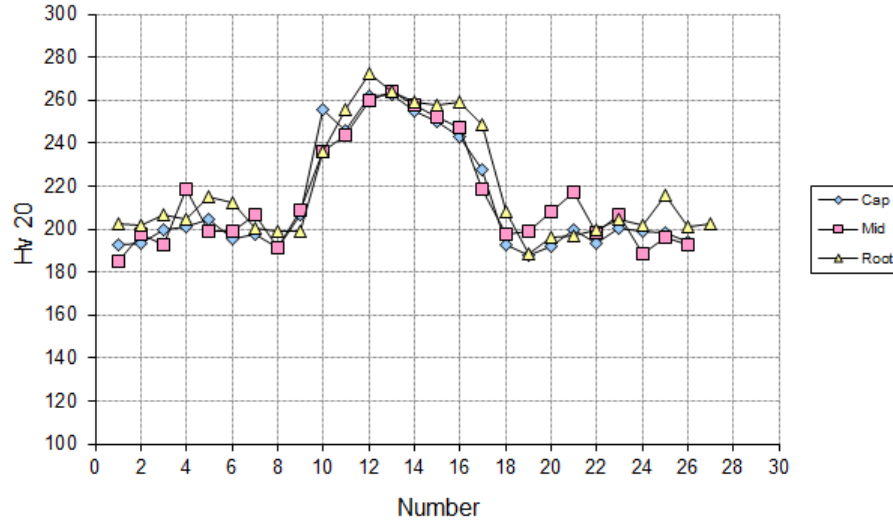


These hardness results can be compared to those performed by TWI on SA508 Grade 3 RPEB welds that underwent a PWHT at TWI as described above and repeated here:  $607\text{ }^{\circ}\text{C} \pm 13\text{ }^{\circ}\text{C}$  in an air furnace for 3.5 h, and cooled at  $20\text{ }^{\circ}\text{C}$  per hour to  $300\text{ }^{\circ}\text{C}$  before still air cooling to ambient temperature [22]. The data shown in Figure 9 are from a 160 mm weld with weld conditions given in Table 3. The hardness testing was performed with a 20 kg load using a diamond pyramid indenter. The hardness data for the two welds, one without PWHT, one with PWHT, are quite similar. The parent metal has a hardness of approximately 195 HV which rises across the HAZ to a hardness of approximately 260 HV across the weld. The effect of the tempering of the weld metal in the PWHT was to reduce the hardness by approximately 30 HV.

The hardness data for the SA 508 Grade 4N sample are overlaid on a photograph of the weld cross-section in Figure 10. The weld metal was approximately 7.6 mm across with approximately 3.2 mm HAZ bands on either side of the weld metal. The hardness in this weld was significantly higher than that in the SA 508 Grade 3. The parent metal hardness was approximately 260 HV, rising across the HAZ, to approximately 500 HV, with hardness results reaching as high as 533 HV. In Figure 10, the orange diamond test points were performed with a 0.3 kg load and the light blue square test points were performed with a 1 kg load.

This finding of high hardness is significant because it may mean that SA 508 4N steel welds that have had similar cooling rates may be susceptible to cracks

Figure 9: TWI Vickers Hardness Traverse of 160 mm SA-508 Grade 3 Weld with PWHT Cross-section [22]



forming before the PWHT. Further, as seen in the TTT diagram for the SA 508 4N in Figure 5, a still slower cooling rate may yield a similar microstructure with comparable hardness, though a slower cooling rate would result in a more bainitic microstructure which has a characteristically lower hardness than that of a martensitic structure for the same steel. Nonetheless, if thick-section SA 508 Grade 4N steel is welded with an electron beam, extra precaution should be taken to ensure that cracks do not form before the PWHT.

Following a PWHT, the hardness of SA 508 Grade 4N RPEB welds is reduced to a more tolerable level. The above results can be compared to those performed by TWI on SA 508 Grade 4N RPEB welds that underwent a PWHT at TWI as described above and repeated here:  $565\text{ }^{\circ}\text{C} \pm 14\text{ }^{\circ}\text{C}$  in an air furnace for 30 h. A cooling rate was not specified [26]. The data shown in Figure 11 are from a 147 mm weld with weld conditions as for the 140 mm weld in Table 3. The hardness testing was also performed with a 20 kg load using a diamond pyramid indenter. The hardness measured spanned from approximately 245 HV in the parent metal, rising through the HAZ, up to approximately 310 HV in the weld zone, with hardness values reaching 320 HV. The PWHT is quite severe, and in this case, so is the tempering of the microstructure, reducing the hardness in the weld metal by approximately 190 HV.

Figure 10: Vickers Hardness Traverse of the SA-508 Grade 4N Weld without PWHT Cross-section

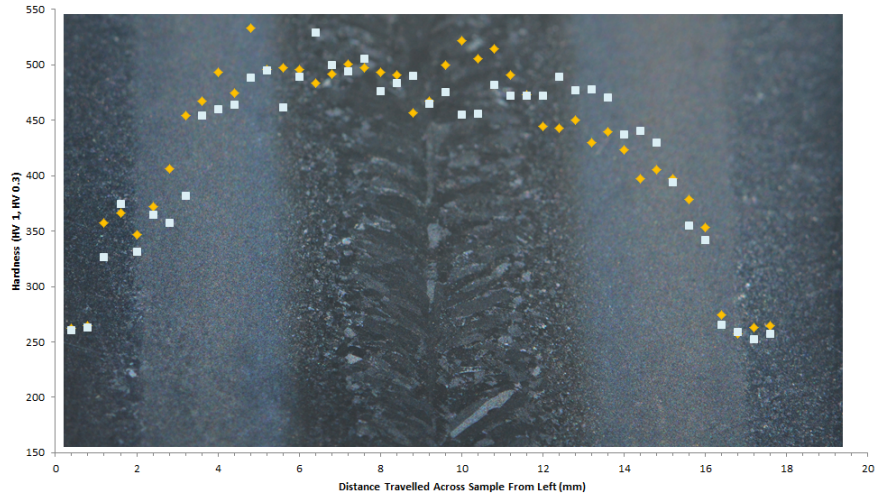
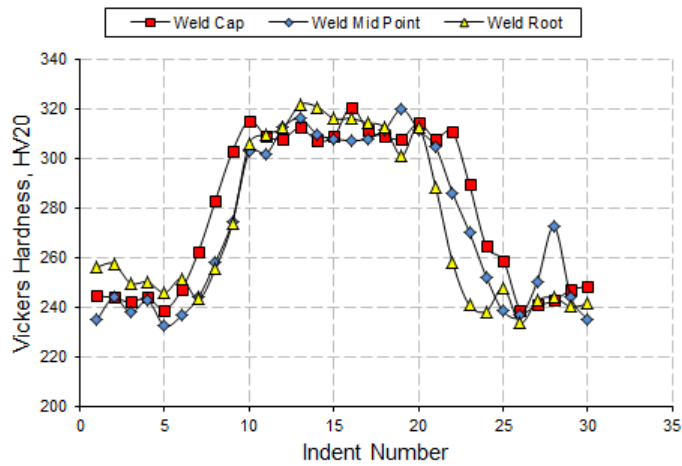


Figure 11: TWI Vickers Hardness Traverse of 147 mm SA-508 Grade 4N Weld with PWHT Cross-section [23]



**Austenite Grain Measurement** Austenite grain measurements were taken by measuring the average-longitudinal cross section, or mean lineal intercept, of many prior austenite grains as revealed by the etching process. The mean lineal intercept in a transverse section  $\bar{L}_{tn}$  relates to the side length,  $a$ , of a hexagonal column, by equation 6. An example set of measurements of  $\bar{L}_{tn}$  are shown in Figure 18. The captions in the figure give the measurements of the indicated grains, from top to bottom, as: 123.1, 189.1, 236.1, and 164.6  $\mu\text{m}$ .

$$\bar{L}_{tn} = \pi a \frac{\cos(30)}{2} \quad (6)$$

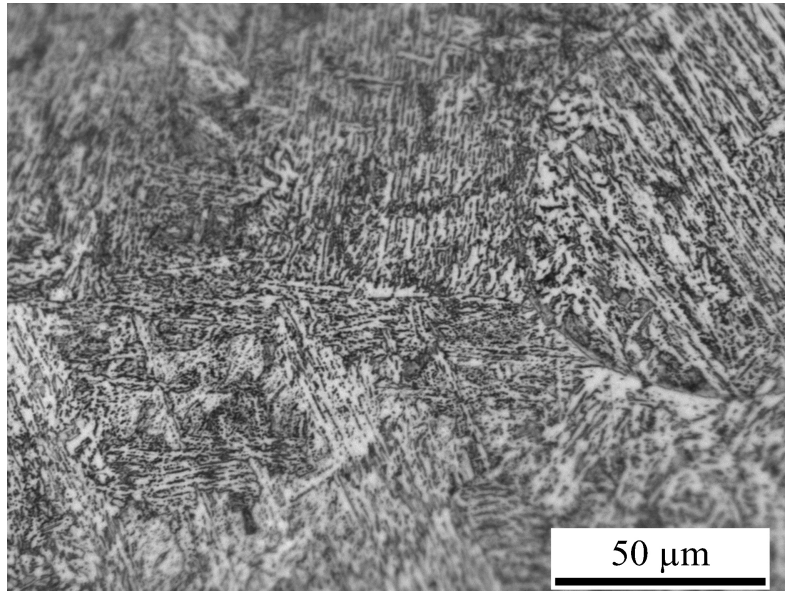
The SA 508 Grade 4N sample was characterized with 70 measurements, with an  $\bar{L}_{tn}$  of 188.6  $\mu\text{m}$  and resulting side length  $a$  of 138.7  $\mu\text{m}$ . Austenite grains were less recognizable in the SA 508 Grade 3 sample, and fewer measurements were able to be taken. The 14 measurements taken gave an  $\bar{L}_{tn}$  of 246.0  $\mu\text{m}$  and resulting side length  $a$  of 180.8  $\mu\text{m}$ . The value  $2a$  was used for each in the mucg65 model, described above.

**Optical Micrographs and Microstructure Interpretation** Over 120 optical micrographs were taken between the two weld samples at low to high resolution. However, none give a definite indication of the microstructure, even at 1000x magnification. The microstructure for each appears to be segregated into two regimes in the weld metal, a transition regime between the weld metal and the HAZ, the HAZ regime, and a transition regime between the parent metal and the HAZ. Though, the regimes appear much more distinct in the SA 508 Grade 4N weld than in the SA 508 Grade 3 weld. These different regimes are potentially consistent with a weld pool that solidifies from small grains of  $\delta$ -ferrite at the fusion boundary, nucleates larger equi-axed  $\delta$ -ferrite grains, and still further nucleates the columnar prisms that grow along the direction of heat flow.

In the SA 508 Grade 3 weld centre shown in figure 12, the dominant structure seems to be composed of sectioned plates 10 to 20  $\mu\text{m}$  across, consistent with martensite. However, there is a significant amount of dotting of the order of 1  $\mu\text{m}$  throughout as well, consistent with a bainitic structure due to the much smaller nature of bainite and its characteristic formations of high aspect ratio structures. Interestingly, the semicircle grain boundary visible on the right hand side of the micrograph seems to have thickened to some small extent, and may indicate the presence of allotriomorphic ferrite. Adjacent the weld centre, in Figure 13, the microstructure is again a mixture of larger plates as consistent with martensite and smaller dotting consistent with bainite, though the relative fraction of bainite seems to be greater here. These optical micrographs, if the interpretations are accurate, do lend support to the volume fraction characterization provided by the mucg65 model regarding the SA 508 Grade 3 weld steel. However, the presence of apparently different microstructure regimes within the weld suggests that the weld metal will have varying properties. Nonetheless, the prediction of 66 percent bainite and 20 percent martensite appears moderately accurate, perhaps underestimating the martensite in the weld centre. The

potential presence of allotriomorphic ferrite also supports the model, though seemingly not at a fraction of 10 percent as predicted.

Figure 12: SA 508 Grade 3 Weld without PWHT Centre 500x Optical Micrograph



In the SA 508 Grade 4N weld centre shown in Figure 14, the microstructure is more difficult to resolve. However, there appear to be plate like structures again, also of the order of 10 to 20  $\mu\text{m}$  across. Similarly, there is some dotting consistent with bainite, though not in significant quantities. The white formations are understood to be the result of chemical segregation and not distinct microstructures. Adjacent the weld centre, in Figure 15, the microstructure appears similar as that for the weld centre, though with smaller prior austenite grains and resulting refinement of the apparent martensite plates. The presence of the dotted structures indicative of bainite is greater here, though still not in significant amounts. The mucg65 model predicted a greater fraction of martensite in the SA 508 Grade 4N than in the SA 508 Grade 3. This seems to be supported by these micrographs, however, the fraction of martensite appears to again be underestimated. The weld centre is potentially nearly entirely martensitic, with a majority fraction of the adjacent region likely being martensitic as well. Similarly, the volume fraction of bainite seems to be overestimated in the weld centre, but may be fairly accurate adjacent the weld centre.

Figure 13: SA 508 Grade 3 Weld without PWHT Weld Metal Mid-Region 500x Optical Micrograph

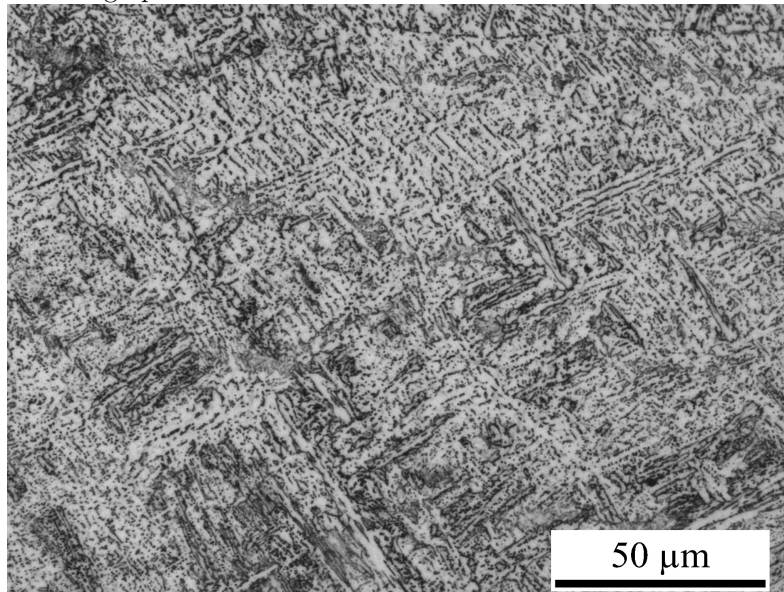


Figure 14: SA 508 Grade 4N Weld without PWHT Centre 500x Optical Micrograph

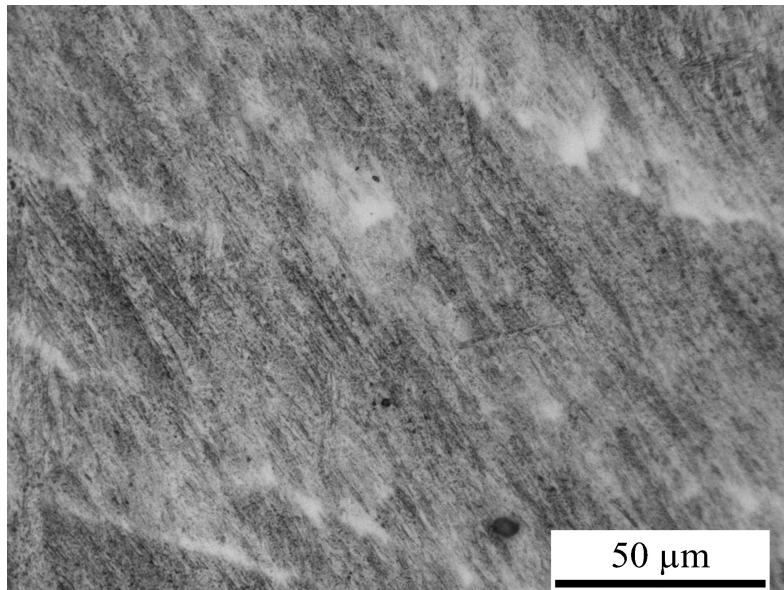
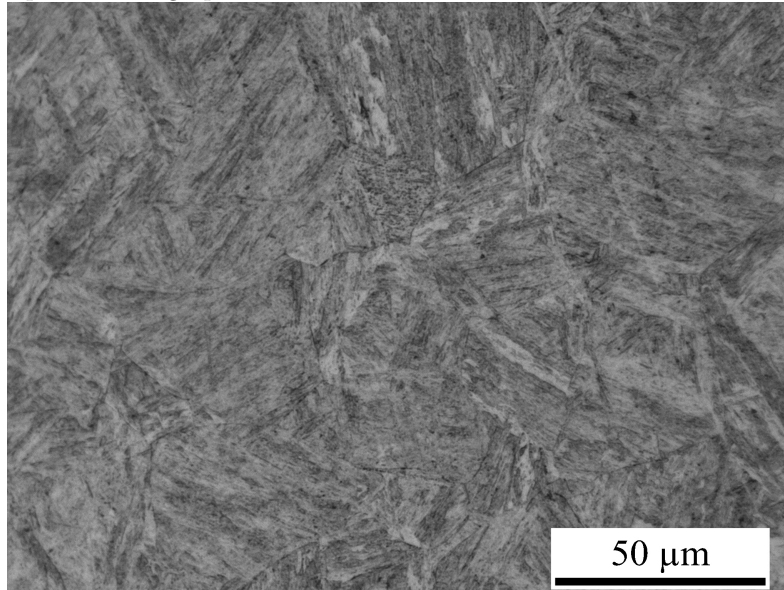


Figure 15: SA 508 Grade 4N Weld without PWHT Weld Metal Mid-Region  
500x Optical Micrograph



### 7.3 Parent Metal Samples

In order to bolster the determination of the microstructure in the SA 508 Grade 3 and SA 508 Grade 4N welds, samples of parent metal from each weld were austenitized and quenched with the intent to form entirely martensitic microstructure. This method was used in [20] and the heat treatments used were based on the heat treatments performed in their work and the thermodynamics data from MTDATA given in Figure 4 [24].

**Heat Treatment** The heat treatments used are given in Table 10, with a full set of 5 samples for both steels. It was seen in [20] that martensite was formed in SA 508 Grade 3 with quench rates greater than  $10\text{ }^{\circ}\text{C/s}$ . Additionally, the degree of austenitization and austenite grain size seemed to play a role in the hardness of the formed martensite, albeit minor and possibly within the margin of error. The different austenitization treatments were used to create a similar range of treatments as [20] and test whether the hardness did in fact differ for fully martensitic microstructures with differing prior austenite grain sizes. One sample of each was air cooled to intentionally form a more bainitic microstructure for comparison. The minimum desired cooling rate of  $10\text{ }^{\circ}\text{C/s}$  was quite certainly achieved using an ice water quench as [20] found a quench rate of  $80\text{ }^{\circ}\text{C/s}$  using water, and the samples sectioned for heat treatment weighed no more than a few grams each.

Table 10: Parent Metal Heat Treatments

Sample	Temperature in °C	Time Elapsed in min	Quench Method
1	1150	10	ice water
2	1150	60	ice water
3	1150	120	ice water
4	1150	120	air
5	1200	60	ice water

**Hardness Testing** The heat treated samples were prepared metallographically as described above, and each were tested on four points at a spacing of 400  $\mu\text{m}$  for hardness with a diamond pyramid indenter and a 1 kg load. The results of the hardness test are shown in Table 11. Interestingly, the austenitized and quenched SA 508 Grade 3 was harder than the SA 508 Grade 4N with the same treatment in the first and last case. Additionally, the length of the treatment certainly had an effect on the resulting hardness for all of the ice water quenched cases, though the trend and reasoning for this is unclear without further heat treatments and measurements. Perhaps important to note is that the hardest samples were those that underwent the least austenitization. Perhaps even faster treatments would yield further harder results.

Noticeably, the the hardest result for the SA 508 4N hardness tests did not achieve near that what it did following the RPEB weld, falling short by approximately 160 HV. Since the data do not compare well with the hardness measured in the weld traverses, they will likely not provide reliable indications of martensitic and bainitic structures other than to show the comparison between the ice water quenched, martensitic hardness and the air cooled, presumably more bainitic hardness.

Table 11: Parent Metal Heat Treated Vickers Hardness Testing

SA 508 Grade 3		SA 508 Grade 4N	
Sample	Average Hardness	Sample	Average Hardness
1	370.8	1	341
2	299.0	2	303
3	279.3	3	299
4	206.3	4	252
5	341.0	5	334

**Optical Micrographs and Microstructure Comparisons** In addition to the hardness testing, optical micrographs were taken of the heat treated parent metal samples so that the certainly martensitic structure in the ice water quenched samples might be visually compared with the potentially martensitic

structures in the welds. Sample 3 of the SA 508 Grade 3 treatment is shown in Figure 16. The structure resembles that of the SA 508 Grade 3 weld metal to some extent, with similar length plates. However, the irregular small, dark regions, unlikely to be bainite due to the ice water quench, are potentially, though unlikely to be, carbides resulting from remaining chemical segregation during the austenitization, and they do not resemble the small dotted structures in the SA 508 Grade 3 weld micrographs. Higher resolution is necessary to make a better determination.

The corresponding optical micrograph of the SA 508 Grade 4N sample 3 is shown in Figure 17. The microstructure appears to be primarily martensitic, and interestingly a sizable fraction of it is coalesced martensite as described in [20]. The plate lengths are similar to those seen in the SA 508 Grade 4N, as is the appearance. However, regions in Figure 17 with phases between the plates are inconsistent with martensite, and further resolution is necessary to make a positive identification.

The micrographs of the ice water quenched martensite structures lend a good deal of confidence to the identification of the martensitic structures in the steel welds. Positively identifying the bainite would require scanning electron microscopy, though the structures in the welds described above are consistent with the expected structures of bainite.

Figure 16: SA 508 Grade 3 Heat Treated Parent Metal Sample 3 Optical Micrograph at 500x

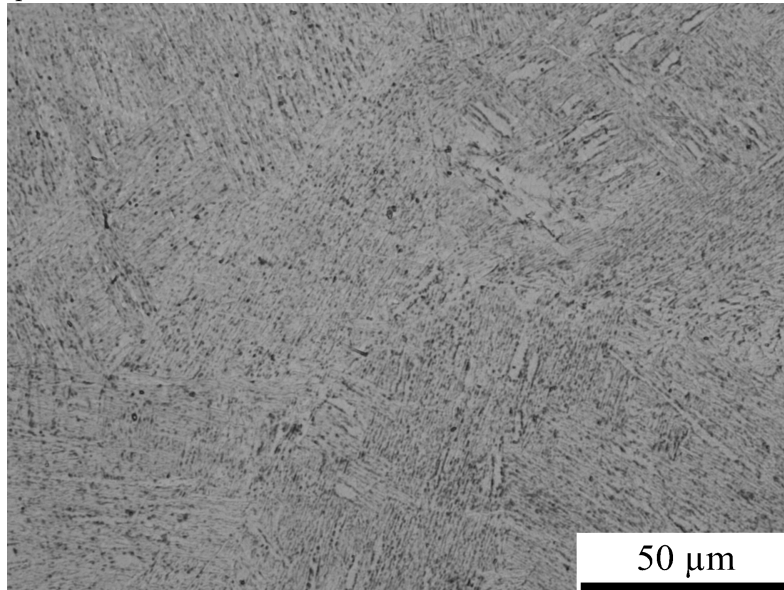
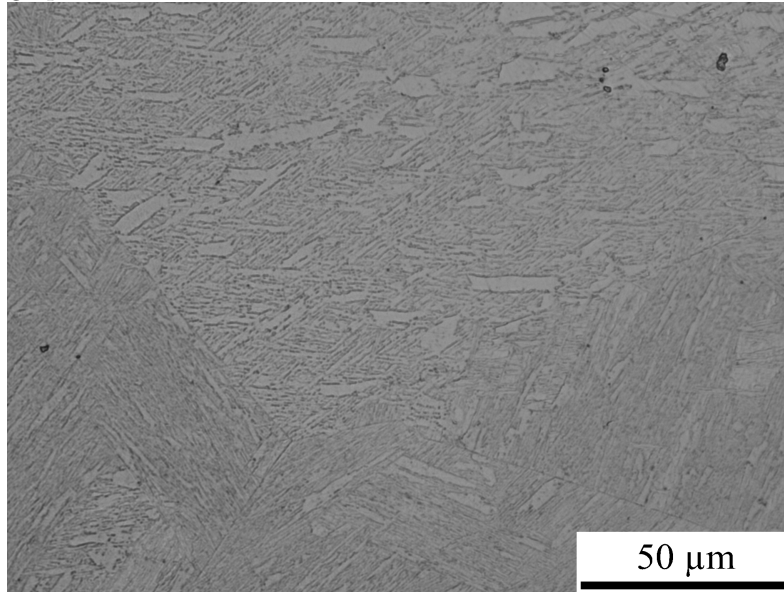


Figure 17: SA 508 Grade 4N Heat Treated Parent Metal Sample 3 Optical Micrograph at 500x



## 8 Conclusion of the Theoretical and Physical Results

The mucg65 model was used to determine the theoretical volume fractions of the microstructures in the as-deposited weld metal resulting from an electron beam welding process. Limited physical validation was possible due to the positive identification of martensitic structures in the welds, likely identification of bainitic structures in the welds, and likely identification of allotriomorphic ferrite in the SA 508 Grade 3 weld. Positive identification for the bainite will require electron microscopy to resolve the very fine structure of bainite plates.

Based on the identifications given, the mucg65 model seems to underestimate the amount of martensite in both welds. A potential and likely cause of this is a cooling curve that underestimates the cooling rate. For example, using coefficients fitted to laser welding - a process that should bear similarities to EB welding due to its high energy density and penetration depth - a much steeper cooling curve is calculated, and resulting greater fraction of martensite. However, only further temperature traces of RPEB welds would help to ensure the accuracy of the fitted cooling curve coefficients  $C_1$  and  $C_2$ .

One important practical consideration arose in the hardness testing of the SA 508 Grade 4N RPEB weld in that it exhibited unusually high hardness, around 500 HV. Such a hard material will likely also be brittle and there is a potential for cracks to form in the weld before the PWHT is applied. This

would likely damage the fracture toughness of the ultimate weld.

## References

- [1] ASTM. Standard specification for quenched and tempered vacuum-treated carbon and alloy steel forgings for pressure vessels A 508/A 508M, 2004.
- [2] N. Bagshaw. Email conversation of 18 August 2014 between Nick Bagshaw of TWI, Luke Burling of Rolls-Royce, and the author.
- [3] H.K.D.H Bhadeshia. Driving force for martensitic transformation in steels. *Metal Science*, pages 175–177, 1981.
- [4] H.K.D.H Bhadeshia. Thermodynamic extrapolation and martensite-start temperature of substitutionally alloyed steels. *Metal Science*, pages 178–180, 1981.
- [5] H.K.D.H. Bhadeshia. Application of first-order quasichemical theory to transformations in steels. *Metal Science*, 16:167–169, 1982.
- [6] H.K.D.H. Bhadeshia. Modelling of steel welds. *Materials Science and Technology*, 8:123–133, 1992.
- [7] H.K.D.H. Bhadeshia. *Bainite in Steels: Microstructure, Transformations, and Properties, 2nd ed.* Institute of Materials, 2001.
- [8] H.K.D.H. Bhadeshia. Steels. [www.msm.cam.ac.uk/phase-trans/2010/m21.pdf](http://www.msm.cam.ac.uk/phase-trans/2010/m21.pdf), 2010.
- [9] H.K.D.H. Bhadeshia and R.W.K. Honeycombe. *Steels: Microstructure and Properties, 3rd ed.* Butterworth-Heinemann, 2006.
- [10] H.K.D.H. Bhadeshia and L.E. Svensson. *Modelling the Evolution of Microstructure in Steel Weld Metal.* Eds. H. Cerjak and K. E. Eastering, Institute of Materials, London, 1993.
- [11] K. Ayres et al. Development of reduced pressure electron beam welding process for thick section pressure vessel welds. *ASME Pressure Vessels and Piping Division Conference*, July 18-22, 2010.
- [12] GetData. GetData Graph Digitizer. <http://www.getdata-graph-digitizer.com/>.
- [13] H.K.D.H. Bhadeshia. mucg65 weld microstructure program.
- [14] H.K.D.H. Bhadeshia, L.E. Svensson, and B. Grestoft. A model for the development of microstructure in low-alloy steel Fe-Mn-Si-C weld deposits. *Acta Metallurgica*, 33:1271–1283, 1985.

- [15] S.A. Khan and H.K.D.H. Bhadeshia. Kinetics of martensitic transformation in partially bainitic 300M steel. *Materials Science and Engineering*, pages 257–272, 1990.
- [16] L.E. Svensson, B. Gretoft, and H.K.D.H. Bhadeshia. An analysis of cooling curves from the fusion zone of steel weld deposits. *Scandinavian Journal of Metallurgy*, 15:97–103, 1986.
- [17] B.S. Lee, M.C. Kim, J.H. Yoon, and J.H. Hong. Characterization of high strength and high toughness Ni-Mo-Cr low alloy steels for nuclear application. *International Journal of Pressure Vessels and Piping*, 87(1):74 – 80, 2010. Seventh International Workshop on the Integrity of Nuclear Components.
- [18] Phase Transformation and Complex Properties Research Group, Department of Materials Science and Metallurgy, University of Cambridge and The National Physical Laboratory. Materials Algorithms Project. <http://www.msm.cam.ac.uk/map/mapmain.html>.
- [19] H. Pous-Romero. Unpublished thesis literature review, 2014.
- [20] H. Pous-Romero and H.K.D.H. Bhadeshia. Coalesced martensite in pressure vessel steels. *Journal of Pressure Vessel Technology*, 136, 2014.
- [21] C. Punshon. Reduced pressure electron beam welding - development of a prototype local vacuum system. *TWI*, 2008.
- [22] C. Punshon. EB welding of thick section RPV materials - ferritic steel - part 1. *TWI*, 2009.
- [23] C. Punshon and N. Bagshaw. EB welding of thick section RPV materials - ferritic steel - part 2 type 4 material. *TWI*, 2010.
- [24] Thermodynamics and Process Modelling Group, NPL Materials Centre, National Physical Laboratory. MTDATA, version 4.73 for LNX RH 7.3, 2002.
- [25] L. Wei and C. Punshon. Mechanical testing of RPEB welded joints in steel forgings. *TWI*, 2009.
- [26] L. Wei and C. Punshon. Mechanical testing of RPEB welded joints in 3.5Ni1.75Cr0.5Mo steel forgings. *TWI*, 2010.

Figure 18: Example Prior Austenite Grain Measurement from SA 508 Grade 4N Sample

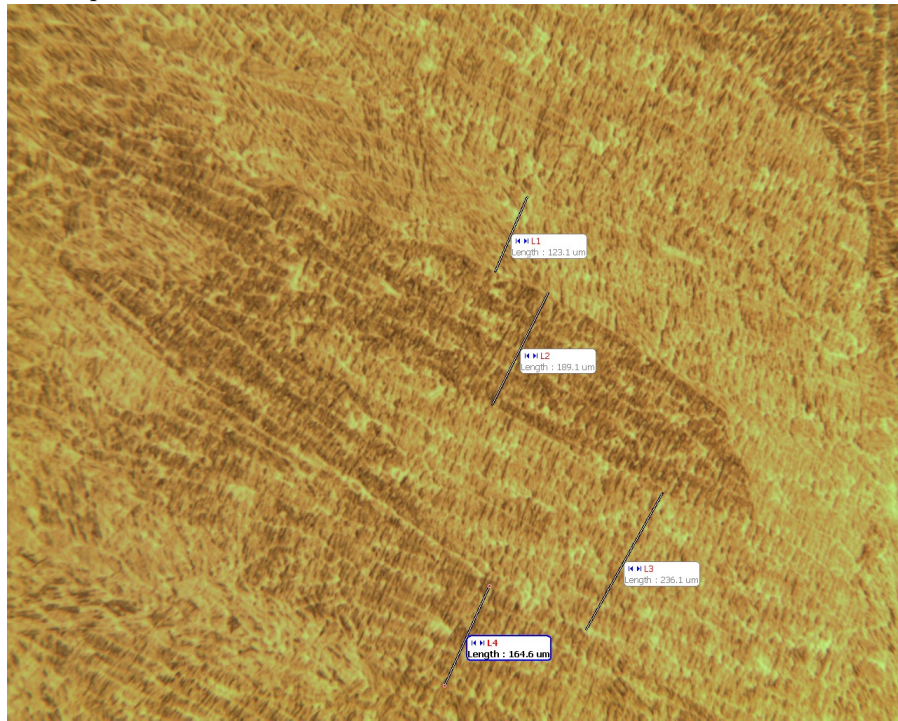


Table 12: mucg65 Model Input Summary

	Measure	SA 508 Grade 3	SA508 Grade 4N
$\gamma$ grain size, a	$\mu\text{m}$	180.80	138.66
Carbon	wt%	0.17	0.22
Silicon	wt%	0.248	0.05
Manganese	wt%	1.382	0.05
Nickel	wt%	0.774	3.69
Molybdenum	wt%	0.52	0.56
Chromium	wt%	0.236	1.92
Vanadium	wt%	0.002	0.002
Nitrogen	wt%	0	0
Boron	ppmw	3	3
Oxygen	wt%	0	0
Aluminum	wt%	0.019	0.008
Titanium	wt%	0.002	0.002
Sulphur	wt%	0.002	0.002
Voltage	kV	150	150
Amps	mA	318	318
Weld Speed	mm/min	100	100